Mixing-induced chemical disequilibrium creates and modifies basaltic crystal cargoes

David A. Neave[1,2]*, Philipp Beckmann[2], Harald Behrens[2] and François Holtz[2]

[1]Department of Earth and Environmental Sciences, The University of Manchester, Manchester, UK

[2]Leibniz Universität Hannover, Institut für Mineralogie, Hannover, Germany

*email: david.neave@manchester.ac.uk

Draft manuscript for submission to Nature Communications.

Abstract (148/150 words)

Main text (4886/5000 words)

Methods (1271/3000 words)

Figures (9/10)

Abstract

Crystal cargoes of oceanic basalts often preserve records of mantle-derived chemical variability that are erased from their carrier melts by magma mixing. However, the impacts of mixing between similarly primitive but chemically variable magmas remain poorly understood despite ubiquitous evidence of chemical variability in primary melt compositions and chemical disequilibrium in erupted crystal cargoes. Here we report observations from magma-magma reaction experiments performed on analogues of primitive Icelandic lavas from chemically and lithologically distinct mantle sources to determine how crystals respond to mixing-induced chemical disequilibrium. Chemical variability in our experimental products is dominantly controlled by major element diffusion in the melt that alters phase equilibria relations and triggers waves of plagioclase resorption in initially plagioclase-saturated magmas. Isothermal mixing of chemically variable oceanic basaltic magmas may thus play a pervasive role in creating and modifying basaltic crystal cargoes by unlocking plagioclase-rich mushes and driving resorption, (re-)crystallisation and solid-state diffusion.

Introduction

Chemical variability in primitive oceanic basalts results from variability in mantle melting processes and mantle source compositions[1,2]. Correlations between the isotopic and incompatible element compositions of erupted basalts reflect how subduction and lithospheric recycling have created isotopic and chemical heterogeneity in the mantle through geological time[3]. Subduction has also created lithological heterogeneity in the mantle that propagates through melting into correlated variability in the major and trace element compositions of erupted basalts[4,5]. An important consequence of this major element variability is that similarly primitive but chemically variable oceanic basalts have different phase equilibria relations under the same pressure–temperature (*P*–*T*) conditions, and therefore evolve along compositionally distinct trajectories[6,7]. However, mantle-derived chemical variability is progressively erased by mixing during magma ascent and evolution[8,9], meaning that erupted basalts are often less variable than the primary melts from which they have evolved and rarely record their initial chemical variability[10]. Fortunately, records of mantle-derived chemical variability are often preserved within crystal cargoes and melt inclusions that are more resistant to mixing-induced re-equilibration than the liquids that carry them to the surface and hence provide vital insights into mantle source compositions and magma reservoir properties[11–14]. Nevertheless, crystal-melt interactions between chemically variable oceanic basalts undergoing mixing are poorly understood, and mixing's role in the creation and modification of basaltic crystal cargoes remains largely unexplored.

Records of mantle-derived variability in basaltic crystal cargoes are associated with disequilibrium features that range from simple concentric zoning to more complex textures indicative of resorption, rapid crystallisation and diffusive re-equilibration[15–17]. Crystal-hosted melt inclusions provide complementary archives that confirm the presence of considerable mantle-derived chemical variability within individual magma plumbing systems[14,18]. Indeed, disequilibrium associated with this chemical variability may play a fundamental role in the formation of some melt inclusion[19,20]. Disequilibrium features in crystal cargoes record changes in magma *P*–*T*–H_2O activity (a_{H_2O})–oxygen fugacity (f_{O_2})–composition (*X*) conditions as well as the timescales over which these changes occur,

and thus enable us to reconstruct magmatic evolution histories. For example, compositional zoning in plagioclase crystals often preserves information about magma reservoir processes and magma transport pathways[21–23], while compositional zoning in olivine crystals can preserve information about timescales of magma storage and ascent[24–26]. Although recharge by hot and primitive magmas often creates disequilibrium features in basaltic crystal cargoes[16,17,27], near-isothermal mixing between chemically variable oceanic basalts can also occur[8,9]. Given that the phase assemblages and phase compositions of basaltic systems with different bulk compositions can differ at a under isothermal contisions[7], isothermal mixing is likely to have important but ill-defined effects on crystal cargoes.

Experimental simulations of magma mixing typically focus on one of the two processes that occur in natural systems: the physical mingling of melts in dynamic experiments[28,29], and the diffusive homogenisation of melts in classic diffusion couples[30,31]. While physical mingling is an essential component of magma mixing, it is diffusive homogenisation that ultimately changes melt compositions and can modify crystal cargoes via resorption, (re-)crystallisation and solid-state diffusion processes. However, melt-melt diffusion couple experiments are typically performed under superliquidus conditions to avoid crystals complicating the characterisation of intra-melt diffusion processes[30,32]; melt-melt diffusion couples provide incomplete insights into magma-magma reactions. Although diffusive controls over crystal growth and resorption have been investigated in some simple systems[33–35], current experiments typically define how pressure and temperature rather than melt composition affect mineral stabilities. Further experiments are therefore required to constrain how crystals respond to changes in melt compositions triggered by magma mixing.

Mantle-derived chemical variability is particularly well characterised in basalts from southwest Iceland. Specifically, incompatible element-depleted basalts from lherzolitic mantle sources have high Al_2O_3 and CaO but low FeO* (total Fe expressed as FeO) and Na_2O contents at any given MgO content, while incompatible element-enriched basalts from recycled mantle sources have low Al_2O_3 and CaO but high FeO* and Na_2O contents[36]. This dichotomy is highlighted by the Háleyjabunga and Stapafell lavas on the Reykjanes Peninsula that constitute compositional end-members (Figs. 1a, 1b)[14]. Crystallisation experiments performed on synthetic analogues of these lavas

illustrate how mantle-derived variability in major element compositions affects phase equilibria relations[7]. Namely, plagioclase crystallises from the Al_2O_3-rich and incompatible element-depleted Háleyjabunga lava analogue at >40 °C higher than it does from the Al_2O_3-poor and incompatible element-enriched Stapafell lava analogue (Figs. 1c, 1d). Thus, incompatible element-depleted magmas crystallise a greater proportion of their mass for any given decrease in temperature than their incompatible element-enriched counterparts, potentially resulting in the deep sequestration of incompatible element-depleted magmas as plagioclase-rich cumulates and the progressive biasing of more evolved magmas towards incompatible element-enriched compositions derived from recycled mantle sources[7]. Moreover, isothermal differences in phase equilibria relations between Háleyjabunga and Stapafell lava analogues suggest that mixing between variably enriched magmas will modify crystal cargoes as the chemically distinct magmas attempt to restore chemical equilibrium. The Háleyjabunga and Stapafell lavas thus represent excellent model systems for investigating how mixing-induced chemical disequilibrium affects the basaltic crystal cargoes and the magma plumbing systems from which they erupt.

Here we present the results of magma-magma reaction experiments designed to determine how mixing-induced chemical disequilibrium affects the crystal cargoes of chemically variable primitive oceanic basalts. Specifically, we investigate how crystals respond to the diffusive re-equilibration of melt major element contents between two chemically distinct magmas. We do this by juxtaposing magma cylinders produced from synthetic analogues of the Háleyjabunga and Stapafell lavas at 300 MPa and 1190 °C for durations of 1 to 96 hours, conditions selected to maximise phase equilibria differences between the two synthetic magmas and ensure that experiments were carried out under realistic magma storage conditions[7,37]. Having defined how crystals respond to the diffusive re-equilibration of their host melts in our experimental system, we explore the implications of our findings for crystal mush stability and the formation of disequilibrium features in natural systems.

Results

Magma synthesis experiments. Magma cylinders were synthesised in Fe-preconditioned $Au_{80}Pd_{20}$ capsules during crystallization experiments performed on dry glass powders of Háleyjabunga and

Stapafell lava analogues. The syntheses were performed in an internally heated pressure vessel (IHPV) at 300 MPa and 1190 °C for 72 hours. The experiments were conducted at low a_{H_2O} (~0.06, equivalent to a melt H_2O content of ~0.7 wt.%[38]) and broadly reducing conditions (approximately one log unit above the fayalite-magnetite-quartz buffer; FMQ+1[39]).

The products of the synthesis experiment performed on the incompatible element-depleted Háleyjabunga lava analogue contain crystals of olivine, clinopyroxene and plagioclase (Fig. 2a), whereas experimental products from the incompatible element-enriched Stapafell lava analogue only contain crystals of olivine and clinopyroxene (Fig. 2b). Although the products of the incompatible element-depleted experiment have a lower average glass content (i.e. melt mass fraction, F) than that the products of the incompatible element-enriched experiment (F = 0.72 and 0.90, respectively, according to mass balance; all phase analyses are provided in the Supplementary Data), glasses are interconnected throughout the products of both synthesis experiments. Crystals are typically euhedral to subhedral, consistent with a close approach to equilibrium, and while some clinopyroxene aggregates occur, degrees of crystal impingement are generally low.

Magma-magma reaction experiments. Magma-magma reaction experiments were performed at exactly the same P–T–a_{H_2O}–f_{O_2} conditions as magma synthesis experiments (300 MPa, 1190 °C, a_{H_2O} ~ 0.06, f_{O_2} ~ FMQ+1) for durations of 1, 4, 24 and 96 hours; they were also performed in the same IHPV. Two ~3 mm-long cylinders of each synthetic magma analogue were juxtaposed in new Fe-preconditioned $Au_{80}Pd_{20}$ capsules. The dense and FeO*-rich Stapafell analogue was always placed at the bottom of the capsule to minimise advective processes during experimental runs[40].

The products of magma-magma reaction experiments retain the textural characteristics observed in the products of magma synthesis experiments (Figs. 3), with crystals being both smaller and more abundant in the products of the incompatible element-depleted Háleyjabunga analogue than in those of the incompatible element-enriched Stapafell analogue. Glass composition profiles through the products of magma-magma reaction experiments have variably linear and sigmoidal forms that depend on the element and experimental duration in question (Fig. 4). Profiles near the central axis of

experimental products have similar forms to those near their rims, meaning that parallel profiles could be stacked following normalisation to common midpoints. Importantly, the similarity of parallel profiles demonstrates that advection was limited once magma-magma interfaces were established and that experimental products hence record dominantly diffusive signals.

Away from initial magma-magma interfaces, glasses from the Stapafell analogue have lower Al_2O_3 contents and higher FeO*, TiO_2 and K_2O contents than those from the Háleyjabunga analogue after short experimental durations of 1 and 4 hours (~14.5, ~11.0, ~1.7 and ~0.22 wt.% versus ~16.0, ~10.0, ~0.75 and ~0.10 wt.%, respectively; Figs. 4a–c, 4e). Differences in CaO and Na_2O contents are also visible after 1 and 4 hours (~12.0 and ~2.1 wt.% versus ~12.6 and ~1.7 wt.%, respectively; Figs. 4c, 4f), but are comparable in magnitude to 2σ analytical uncertainties (±0.44 and ±1.3 wt.%, respectively). SiO_2 and MgO contents do not vary significantly between the two magma analogues and are not shown in Fig. 5 (full phase compositions are provided in the Supplementary Data). Al_2O_3 TiO_2 and K_2O profiles have sigmoidal forms that show progressively more gradual transitions between the starting glass compositions with increasing experimental duration (Figs. 4a, 4c, 4e). FeO* profiles are sigmoidal in the products of 1- and 4-hour experiments, but linear in the products of 24- and 96-hour experiments (Fig. 4b). FeO* contents are also displaced to lower mean FeO* contents in the products of the 24- and 96-hour experiments, possibly as a result of Fe loss to $Au_{80}Pd_{20}$ capsules in these experiments[41]. CaO and Na_2O profiles are linear and CaO and Na_2O contents do not vary beyond analytical uncertainties in the products of 24- and 96-hour experiments, (Figs. 4d, 4f).

Diffusive re-equilibration of experimental glasses. Stacking glass composition profiles by normalising distances through experimental products by square roots of experimental durations demonstrates that glass compositions are primarily controlled by diffusive re-equilibration between chemically distinct melts in the starting magma analogues (Fig. 5)[31,42]. This is because diffusion distance scales with the square root of the diffusion coefficient multiplied by the diffusion time (i.e. $x \propto \sqrt{Dt}$, where x is the diffusion distance, D is the diffusion coefficient and t is time)[42], meaning that composition profiles will overlap once the effects of diffusion over different durations is taken into account (assuming that diffusion coefficients remain constant)[31]. Key implications of the

overlapping time-normalised glass composition profiles shown in Fig. 5 are that diffusion appears to have operated coherently during all of our magma-magma reaction experiments and that observations from the products of different experimental runs may thus be meaningfully compared with each other.

Effective binary diffusion coefficients estimated by fitting error functions through glass composition profiles to solve Fick's 2nd Law are consistent with the modest body of published values available (Fig. 6)[32–35,43–45]. Most published diffusion coefficients for basaltic melts have been derived from crystal dissolution experiments[33–35] or classic melt-melt diffusion couples[32,43]. Na diffusivity has also been estimated from radiotracer diffusion experiments[44]. Where error functions can be fitted to our glass composition profiles, our effective binary diffusion coefficients are typically within one ln unit of regressions through global datasets that follow Arrhenian relationships ($D = D_0 e^{-E_A/RT}$, where D is the diffusion coefficient, D_0 is the pre-exponential factor, E_A is the activation energy for diffusion and R is the gas constant; Fig. 6). Diffusion coefficients estimated from 1- and 4-hour experiments are particularly close to global regressions for Al_2O_3, FeO* and CaO (r^2 = 0.83, 0.92 and 0.79 respectively), suggesting that the behaviour of these elements in basaltic melts can be largely explained without complex multicomponent diffusion models (Figs. 6a, 6b, 6d). While our estimated diffusion coefficients for TiO_2 are similar to published values, the latter span three ln units at any given T and global regression statistics are modest (r^2 = 0.59), suggesting that TiO_2 diffusion may be more strongly affected by matrix effects than the diffusion of other elements (Fig. 6c). Although published diffusion coefficients are scarce for K_2O and Na_2O[43,44], our estimates fall on plausibly Arrhenian trends with the few data available (Fig. 6e, 6f). Estimated diffusivities of Al_2O_3 and TiO_2 are similar to theoretical Eyring diffusivities that relate diffusion coefficients to temperature and melt viscosity an perform well when describing the behaviour of network-forming cations an oxygen ($D_E = k_B T/\lambda\eta$, where D_E is the Eyring diffusivity, k_B is Boltzmann's constant, λ is a jump distance of 0.4 nm related to the atomic spacing of silicate liquids and η is the average viscosity of the two end-member melts, calculated here with the model of Giordano et al.[46])[31,47]. In contrast, estimated diffusivities of Na_2O and, to a lesser extent, K_2O are higher, possibly reflecting differences in diffusion mechanisms between network-forming and network-modifying cations (Figs. 6)[48,49].

Mineral stabilities and compositions. Olivine crystals are present in the products of magma synthesis experiments on both lava analogues (Fig. 2, 7a). However, they have higher forsterite contents [X_{Fo} ~ 0.852 versus 0.843, respectively, where X_{Fo} = Mg/(Mg+Fe) on a molar basis] in the products of the experiment on the FeO*-poor Háleyjabunga analogue than the products of the experiment on the FeO*-rich Stapafell analogue. This difference in olivine compositions is reflected by X_{Fo} steps across magma-magma interfaces in the products of 1- and 4-hour experiments (Fig. 7a). Steps in X_{Fo} also occur in the products of 24- and 96-hour experiments but are less prominent than those in the products of the 1- and 4-hour experiments as a consequence of the olivine undergoing diffusive re-equilibration in response to Fe loss (24-hour experiment in particular) and diffusive homogenisation of melt FeO* contents (96-hour experiment in particular). Indeed, some olivine crystals from these experiments appear to show diffusion profiles (Supplementary Fig. 1).

Plagioclase crystals are present in the products of the synthesis experiment on the Háleyjabunga analogue; plagioclase is absent from the products of the synthesis experiment on the Stapafell analogue (Fig. 2 7b). In line with published phase equilibria relations[7], these crystals have high anorthite contents [X_{An} ~ 0.83, where X_{An} = Ca/(Ca+Na) on a molar basis]. Similarly, plagioclase is only stable within the portions of magma-magma reaction experiments derived from the Háleyjabunga lava analogue. Although X_{An} variability exceeds analytical uncertainty in the products of all magma-magma reaction experiments, mean X_{An} does not vary systematically as a function of position or experimental duration. In contrast, plagioclase stability depends strongly on experimental duration. While plagioclase is stable throughout the portion of the 1-hour experiment derived from the synthesis experiment on the Háleyjabunga lava analogue (Fig. 3a), the region where plagioclase is stabile progressively shrinks as experimental duration increases (Fig. 3b–d), leaving a >1-mm broad region of plagioclase resorption in the products of 24- and 96-hour experiments. Projecting regions of plagioclase stability onto time-normalised composition profiles indicates that plagioclase resorption occurs when melt Al_2O_3 contents are lowered below ~16 wt.% by diffusive re-equilibration in the melt (Fig. 5a). The region of plagioclase stability in the products of 24-hour experiments is smaller than expected from comparisons with the products of other experiments, which we attribute to the

aforementioned modification of melt compositions by Fe loss leading to corresponding increases in other melt components including Al_2O_3. Nevertheless, our experiments indicate that plagioclase stability is dominantly controlled by melt Al_2O_3 content (and thus melt Al/Si) rather than melt CaO and Na_2O contents (and thus Ca/Na) as both CaO and Na_2O diffuse considerably faster than Al_2O_3 in both our experimental system and basaltic melts more generally (Fig. 6)[45].

Clinopyroxene crystals are present in the products of synthesis experiments on both lava analogues (Fig. 2). While much variability in clinopyroxene Mg-number [$Mg\#_{cpx}$, where $Mg\#_{cpx}$ = Mg/(Mg+Fe) on a molar basis] is related to sector zoning in experimentally produced clinopyroxene crystals[50], a slight difference in mean $Mg\#_{cpx}$ between the products of the experiments on the Háleyjabunga and Stapafell analogues ($Mg\#_{cpx}$ ~ 0.835 versus 0.850, respectively) reflects differences in their melt FeO* contents (Fig. 7c). However, differences between the two magma analogues are more clearly expressed in terms of clinopyroxene TiO_2 contents, with clinopyroxene crystals grown from the incompatible element-enriched Stapafell analogue containing considerably more TiO_2 than those grown from the incompatible element-depleted Háleyjabunga analogue (TiO_2 ~ 0.48 versus 0.28 wt.%, respectively; Fig. 7d). Chemical variability associated with clinopyroxene sector zoning masks $Mg\#_{cpx}$ steps across magma-magma interfaces in the products of magma-magma reaction experiments ($Mg\#_{cpx}$ steps of ~0.01 are difficult to resolve within total $Mg\#_{cpx}$ ranges of 0.825-0.855, Fig. 7c). Nevertheless, overall gradients of low $Mg\#_{cpx}$ in the Stapafell analogue increasing to high $Mg\#_{cpx}$ in the Háleyjabunga analogue can be resolved. In contrast, steps in clinopyroxene TiO_2 contents between magma analogues are much more distinct (from TiO_2 ~ 0.2–0.3 wt.% in portions from the Háleyjabunga analogue to 0.4–0.6 wt.% in portions from the Stapafell analogue; Fig. 7d), consistent with the slow diffusion of TiO_2 within clinopyroxene preventing intra-crystalline re-equilibration over the duration of our experiments[51]. Positions of TiO_2 steps do, however, vary with experimental duration, with high-TiO_2 clinopyroxene crystals seemingly replacing low-TiO_2 clinopyroxene crystals in the portion of the Háleyjabunga analogue adjacent to magma-magma interfaces in the products of longer duration experiments. Overall, regions of increased clinopyroxene TiO_2 content largely overlap with regions of plagioclase resorption, feasibly reflecting the complete

resorption and re-crystallisation of clinopyroxene crystals, which may also be related to the diffusive re-equilibration of melt Al_2O_3 contents, though further work will be required to clarify this.

Discussion

Diffusive controls over melt compositions. Although physical mingling is vital for homogenising mantle-derived chemical variability in primitive basalts undergoing mixing, chemical diffusion is ultimately required for mixing to reach completion. Our magma-magma reaction experiments suggest that chemically variable magmas must be mechanically thinned to filaments no more than a few mm wide for diffusive homogenisation to be achieved within the day-to-week timescales typically associated with mixing processes in basaltic plumbing systems[24,25]. Indeed, chemical variability in olivine-hosted melt inclusions from individual eruptions reflects the entrapment of variably mixed melts[8,13], suggesting that crystallisation and diffusive homogenisation of melt compositions occur over broadly consistent timescales. However, our experiments also suggest that mixing can create chemical anomalies by fractionating elements with different diffusivities (e.g., K_2O from TiO_2) that are capable of complicating records of mantle-derived chemical variability. There is compelling evidence that mixing induces diffusive fractionation in low-*T* evolved systems that are predisposed to preserve diffusive features[31,52,53], though little comparable evidence has yet been presented for mixing-induced diffusive fractionation in high-*T* primitive systems. Diffusive fractionation has however been implicated in the creation of high field strength elements depletions in some plagioclase-hosted melt inclusions from oceanic basalts[19,20], and it is at the µm-scale of melt inclusions that it is likely to have its greatest effects. Thus, even transient modifications of melt compositions by diffusion can fundamentally alter our understanding of magmatic processes if they are captured by the melt inclusion archives upon which geological interpretations are often based[54].

The effective binary diffusion coefficients we estimate are not significantly affected by the presence of moderate crystal proportions (crystal mass fractions of 0.1–0.3). Error function fits through glass composition profiles reproduce compositions from crystal-rich portions of experimental products equally well as those from crystal-poor portions (Supplementary Fig. 2), and diffusivities estimated from these fits are consistent with those estimated from melt-only systems (Fig. 6)[32–35,43,44].

Furthermore, melt compositions close to magma-magma interfaces are not detectably affected by either plagioclase resorption or clinopyroxene re-crystallisation; melt compositions in magma-magma reaction experiments are dominantly controlled by diffusion within the melt, with Fe loss imposing second-order controls in longer-term experiments. Our experiments thus suggest that the diffusive homogenisation of crystal-bearing basaltic liquids can be meaningfully approximated by the diffusive re-equilibration of pure melts.

Mineral responses to diffusive changes in melt compositions. Primitive oceanic basalts inherit considerable chemical variability from the mantle[3–5], meaning that different mantle melt batches can have different bulk compositions at similar temperatures and degrees of magmatic evolution[8,9]. As a consequence, isothermal mixing between chemically variable magmas is just as likely to occur as mixing between cool magmas residing within magma reservoirs and hot recharge magmas[16,17,24,27]. Thus, crystal cargoes will not only experience recharge-induced changes in magma temperature but also mixing-induced changes in magma chemistry that occur under near-isothermal conditions.

Plagioclase crystals in magma-magma reaction experiments responded to diffusion-induced changes in local melt compositions by resorbing completely within a few hours. While plagioclase crystals in the products of the magma synthesis experiment on the Háleyjabunga analogue are generally euhedral and tabular (Fig. 2a), those at limits of plagioclase stability in the products of magma-magma reaction experiments are anhedral, embayed and sometimes skeletal (Fig. 8). Our magma-magma reaction experiments have therefore captured plagioclase resorption in action. Specifically, plagioclase mass fractions decrease from far-field values of 0.11 to zero over intervals of no more that ~200 μm that host the most embayed and skeletal plagioclase crystals observed. The small scales of these intervals imply that plagioclase stability in our magma-magma reaction experiments was controlled by the kinetics of Al_2O_3 diffusion in the melt rather than the kinetics plagioclase resorption at crystal-melt interfaces. In other words, the distribution of plagioclase crystals in our experimental products indicates that once local melt Al_2O_3 contents dropped below ~16 wt.%, plagioclase crystals on order of 20 μm long resorbed completely within no more than a few hours. Encouragingly, this observation is consistent with published experiments on anorthite resorption

kinetics, demonstrating that plagioclase crystals can be easily resorbed by mixing-induced changes in melt composition at rates in excess of 10 μm/hour[35].

Olivine and clinopyroxene crystals also responded to diffusion-induced changes in local melt compositions in our experimental products, but in different ways from plagioclase crystals. The development of compositional zoning in olivine crystals from longer-duration experiments suggests that they, at least in part, responded to isothermal changes in melt composition by diffusive re-equilibration in the solid state (Fig. 7a; Supplementary Fig. 1). Nevertheless, we note that some crystals close to magma-magma interfaces are subhedral, which implies that some textural maturation by resorption and crystallisation also occurred (Fig. 8). The partial re-equilibration of olivine crystals over lengthscales of 10–100 μm within timescales of 96 hours is consistent with the relatively fast Mg–Fe interdiffusion in olivine[55], and provides independent validation of mixing timescales estimated from diffusion profiles in natural systems[25]. In contrast, clinopyroxene crystals seemingly responded to changes in local melt composition by resorption and re-crystallisation, as evidenced by steps in clinopyroxene TiO_2 content that progressively invade Háleyjabunga analogues with increasing experimental durations (Fig. 7d). Importantly, these steps in clinopyroxene TiO_2 content are offset from magma-magma interfaces, indicating that they cannot have resulted from convection within experimental capsules. Moreover, clinopyroxene is denser than the H_2O-poor basaltic melts considered here (~3.3 versus ~2.7 g/cm^3), confirming that high-TiO_2 clinopyroxene could not have floated from the Stapafell analogue into the overlying Háleyjabunga analogue. However, the implications of our experimentally observed clinopyroxene re-crystallisation for natural systems remain unclear, partly because the small size of experimental crystals (typically <10 μm in length) makes it difficult to gauge how larger crystals would respond in nature. It is nevertheless plausible that well-documented instances isobaric clinopyroxene resorption in natural basalts may reflect resorption triggered by changes in magma chemistry as well as in magma temperature[12,56].

Magma mixing creates and modifies basaltic crystal cargoes. Crystal mush disaggregation plays a major role in creating the crystal cargoes carried by many oceanic basalts[13,57,58], and the eruption of plagioclase glomerocrysts with textures reminiscent of igneous cumulates is often interpreted as

evidence for pre-eruptive mush entrainment[21–23]. Although numerical models provide vital insights into the behaviour of crystal-rich magmas[59], the processes by which intergrown and cohesive mushes disaggregate remain largely unclear. For example, the primitive crystal cargoes carried by many oceanic basalts are generally too refractory to have been thermally by the evolved melts that carry them to the surface[13,22,57]: Assuming magma evolution along a single liquid line of descent, liquids in equilibrium with relatively evolved plagioclase crystals ($X_{An} \leq 0.7$) could not resorb grain boundaries in mushes dominated by primitive plagioclase crystals ($X_{An} > 0.8$) formed during earlier phases of higher temperature crystallisation. However, primitive crystal cargoes and evolved carrier liquids are often derived from chemically distinct primary melt distributions[22,60,61]. This means that mush crystals may have never been in equilibrium with melts directly related to their eventual carrier liquids and that grain boundary resorption could be driven by isothermal differences in melt chemistry as much as by differences in melt chemistry coupled with differences in magma temperature.

Crystal mush disaggregation in many basaltic systems may be triggered by chemical disequilibrium associated with the injection of plagioclase-undersaturated magmas into plagioclase-saturated magma reservoirs. Very few basalts erupted in oceanic settings are in equilibrium with high-X_{An} plagioclase at any stage of their evolution[13,57,62]. Instead, high-X_{An} plagioclase in oceanic settings likely crystallises from incompatible element-depleted primitive melts that are correspondingly enriched in refractory elements like CaO and Al_2O_3 and rarely survive crustal processing to erupt at the surface[7,62]. As demonstrated by our magma-magma reaction experiments, the isothermal injection of incompatible element-enriched magmas into reservoirs containing incompatible element-depleted magmas can trigger plagioclase resorption in response to local in melt compositions (Figs. 4, 8). We thus suggest that chemical rather than thermal disequilibrium may play an important role in triggering crystal mush disaggregation in some magma reservoirs. Specifically, we propose that mixing-induced changes in melt compositions modify phase equilibria relations to the point where the plagioclase (and possibly clinopyroxene) grain boundaries that bind primitive mushes together can start to resorb (Fig. 9a). As a consequence, resorption-facilitated mush disaggregation could occur in response to transient changes in local melt compositions caused by even volumetrically minor injections of

incompatible element-enriched magma into large and incompatible element-depleted reservoirs. Furthermore, the effects of chemical disequilibrium will be greatest close to loci of magma injection, creating positive feedbacks between the chemical and physical processes responsible for mush disaggregation and crystal entertainment.

Chemical and isotopic disequilibria between basaltic melts and high-X_{An} plagioclase crystals suggest that chemical variability plays a widespread role in driving crystal mush disaggregation and creating basaltic crystal cargoes. Chemical disequilibrium is well documented in plagioclase ultraphyric basalts from ocean islands and slow- and intermediate-spreading mid-ocean ridges[22,60,61]. This is probably because plagioclase ultraphyric basalts typically erupt in locations without long-lived melt lenses capable of efficiently filtering eruption products and erasing mantle-derived chemical variability[63]. Nevertheless, the occurrence of mush-derived plagioclase crystals in oceanic basalts from diverse settings that include fast-spreading mid-ocean ridges suggests that the disaggregation processes we describe may operate on a global scale[23,64,65]. Finally, we note that variations in the H_2O content of arc magmas may have analogous effects to variations in the major element content of oceanic basalts, whereby the injection of H_2O-rich magmas or fluids into H_2O-poor reservoirs may facilitate mush disaggregation by triggering plagioclase resorption[66].

Regardless of their origins, crystal cargoes will be modified as they interact with liquids in equilibrium with different phase assemblages and different phase compositions as a result of magma mixing, with different mineral phases responding in different ways. The transfer of high-X_{An} plagioclase crystals between melts with different CaO and Al_2O_3 contents can result in either resorption or crystallisation depending on the direction of transfer. For example, our magma-magma reaction experiments demonstrate how the diffusive equilibration of incompatible element-depleted and plagioclase-saturated magmas with incompatible element-enriched and plagioclase-undersaturated magmas can trigger isothermal plagioclase resorption (Figs. 4, 8). However, it is straightforward to envisage slightly different scenarios in which diffusive influxes of Al_2O_3 into incompatible element-enriched magmas instead trigger waves of crystal nucleation in systems close to plagioclase saturation or waves of rim growth in systems that are already saturated in plagioclase.

Although decompression, primitive recharge and boundary layer effects doubtlessly contribute towards the textural complexity of plagioclase crystals in oceanic basalts[13,17,21,23], it is that clear that isothermal and isobaric changes in melt composition are also capable of significantly modifying crystal textures. Furthermore, mixing-induced changes in melt composition present a compelling mechanism for driving the cycles of resorption and re-crystallisation implicated in the formation of plagioclase-hosted melt inclusions from oceanic settings[19,20]. Although correlated changes in temperature and melt composition drive the largest diffusive changes in olivine X_{Fo} contents[24–26], variations in olivine X_{Fo} can also reflect isothermal variations in melt chemistry (Fig. 9c). Indeed, our experiments demonstrate that olivine crystals may largely respond to changes in melt composition by diffusive re-equilibration rather than re-crystallisation. Conversely, our observations suggest that clinopyroxene crystals can respond to changes in melt composition by resorption and re-crystallisation (Fig. 9c), though more work is required to understand the rates and mechanisms by which this occurs. Some of the textural complexity observed in natural clinopyroxenes may nevertheless result from mixing between chemically distinct primitive melts[12,56].

Magma mixing creates and modifies basaltic crystal cargoes and can therefore alter magmatic plumbing system dynamics and erupted records of mantle-derived chemical variability. Crystal resorption in response to mixing-induced chemical disequilibrium represents an underappreciated yet potentially widespread mechanism for disaggregating crystal mushes that can also alter the viscosity, density and eruptibility of oceanic basalts through the entrainment of buoyant high-X_{An} plagioclase crystals[22,57]. Magma mixing not only creates crystalline records of chemical variability through the crystallisation of concentric zones and the entrapment of melt inclusions but also destroys them through resorption, re-crystallisation and solid-state diffusion. Overall, isothermal mixing between chemically variable primitive magmas likely plays an equally important role in generating the texturally and chemically complex crystal cargoes we observe at the surface as more widely recognised processes invoking mixing between variably evolved and thermally distinct magmas.

Methods

Experimental methods. Synthesis experiments were performed in an internally heated pressure vessel (IHPV) in the Institut für Mineralogie of the Leibniz Universität Hannover. Experiment were performed at 300 MPa and 1190 °C to maximise differences in resulting phase assemblages and proportions according to published equilibrium phase relations[7]. Synthetic analogues of the incompatible-element depleted Háleyjabunga and incompatible element-enriched Stapafell lavas were prepared by Neave et al.[7] from reagent grade oxide and carbonate powders that were fused twice in Pt crucibles placed in a muffle furnace at 1600 °C. Each fusion was performed for 1 hour, after which fused powders were quenched by pouring them onto clean brass plates. Quenched glass chips were then powdered in an agate disc mill to ensure that starting materials were compositionally homogenous. About 300 mg of each powdered starting material was then loaded into $Au_{80}Pd_{20}$ capsules with external and internal diameters of 2.6 and 2.2 mm, respectively, and welded shut. Each capsule was ~2.5 mm long in order to maximise the volumes of synthetic magmas that could be produced in a single IHPV experiment. Prior to being loaded with starting materials, capsules were preconditioned with ~0.25 wt.% Fe to minimise Fe exchange between capsules and experimental samples[67] following the procedures described by Husen et al.[68].

Prepared capsules were suspended from a Pt wire in the hot zone of an IHPV[69]. The IHPV was then pressurised to 300 MPa with Ar and heated to 1190 °C. Pressure was monitored with a strain gauge manometer and did not vary by more than 5 MPa; temperature was monitored with four unsheathed S-type thermocouples and did not vary by more than 5 °C. Experimental temperatures were approached by heating the furnace from the room temperature to 10 °C below the target temperature at a rate of 50 °C/min; final heating from 1180 to 1190 °C was performed at a rate of 10 °C/min to avoid overshooting. For the magma synthesis experiments, thermal cycling (1190 ± 5 °C) was applied for the first 24 hours to promote the growth of large crystals[70]. Temperature was then kept constant for the last 48 hours. Experimental products were quenched after 72 hours by fusing the Pt wire on which the capsules were suspended. The capsules dropped into a cold zone at the

bottom of the vessel cooled at a rate of ~150 °C/s, which was sufficient to avoid the formation of quench crystals.

All experiments were conducted under nominally dry conditions (no H_2O was added to the dried starting powders), which resulted in melt H_2O contents of ~0.7 wt.% following the reduction of Fe_2O_3 in the starting glasses to FeO and the inward diffusion of trace H_2 from the Ar pressure medium at high temperatures. These H_2O contents are consistent with the experiments having been run under broadly reducing conditions about one log unit above the fayalite-magnetite-quartz redox buffer (FMQ+1): melt H_2O contents of ~0.7 wt.% correspond to an a_{H_2O} of ~0.06[38], which is related to the $f_{O_2}^{sample}$ by the relationship $f_{O_2}^{sample} = f_{O_2}^{vessel} \cdot a_{H_2O}{}^2$, where $f_{O_2}^{vessel}$ is equivalent to FMQ+3.3[39].

Magma-magma reaction experiments were performed under exactly the same conditions as synthesis experiments, and in the same IHPV. The products of each synthesis experiment were cut into four cylinders ~3.5 mm long. The ends of the products of each synthesis experiment were retained to determine the phase assemblages and phase compositions present at the start of magma-magma reaction experiments. Magma cylinders from each synthesis experiment were then juxtaposed within new $Au_{20}Pd_{20}$ capsules with the same dimensions and Fe contents as those used for synthesis experiments. Each capsule was then welded shut and magma-magma reaction experiments were performed in the same way as described for synthesis experiments. Capsules were oriented with cylinders synthesised from the dense and FeO*-rich Stapafell lava analogue beneath those synthesised from the less dense and FeO*-poor Háleyjabunga lava analogue to prevent intra-capsule convection[40]. Magma-magma reaction experiments were performed for durations of 1, 4, 24 and 96 hours in order to capture the time-dependent nature of kinetic processes. The products of magma-magma reaction experiments were cut longitudinally and mounted in resin alongside the reserved products of synthesis experiments for subsequent imaging and analysis.

Analytical methods. Experimental products were imaged by field emission gun scanning electron microscopy (FEG-SEM) on a JEOL JSM-7610F instrument in the Institut für Mineralogie of the Leibniz Universität Hannover. Backscatter electron images (BSE) were typically collected using an

accelerating voltage of 15 kV and a working distance of 15 mm. BSE maps of experimental products were acquired using the ESPRIT software from Bruker.

The major and minor element compositions of experimental products were determined by electron probe microanalysis (EPMA) on a Cameca SX100 instrument in the Institut für Mineralogie of the Leibniz Universität Hannover. Silicon, Ti, Al, Cr, Fe, Mn, Mg, Ca, Na, K and P were measured in glasses with a beam size of 12 µm, an accelerating voltage of 15 kV and a current of 10 nA. Silicon, Ti, Al, Cr, Fe, Mn, Mg, Ca, Na and K were measured in minerals with a beam size of 1 µm, an accelerating voltage of 15 kV and a current of 15 nA. Elements were counted on peak for 20 s, with the exceptions of Si and Na that were counted on peak for 10 s to minimise detector drift and Na migration, respectively. Background counting times were half on-peak counting times. The following standards were used for calibration: wollastonite (Si and Ca), TiO_2 (Ti), jadeite (Al), Cr_2O_3 (Cr), Fe_2O_3 (Fe), Mn_3O_4 (Mn), MgO (Mg), albite (Na), orthoclase (K) and apatite (P). The following secondary standards were regularly analysed to correct for inter-session drift and to monitor accuracy and precision: VG-2 basaltic glass (NMNH 111240-52; using the preferred MgO content), Kakanui augite (NMNH 122142; using preferred values), San Carlos olivine (NMNH 111312-44) and Lake County plagioclase (NMNH 115900)[71]. Accuracy and precision were typically better than 2% and 2%, and 10% and 10% for major (>1 wt.%) and minor (<1 wt.%) elements, respectively. Typical analyses of standards are provided alongside analyses of experimental products in the Supplementary Data.

Glass H_2O contents were determined in the products of the synthesis experiments and 1- and 96-hour magma-magma reaction experiments by Fourier-transform infrared (FTIR) spectroscopy with a Bruker IFS88 instrument at the Institut für Mineralogie of the Leibniz Universität Hannover following the methods described by Husen et al.[68]. Estimated glass H_2O contents are provided in the Supplementary Data with further information about experimental a_{H_2O}–f_{O_2} conditions.

Estimating effective binary diffusion coefficients. Effective binary diffusion coefficients (D) were estimated by fitting error functions to glass composition profiles through the products of magma-

magma reaction experiments to solve Fick's 2nd Law: $C(x,t) = C_1 + \frac{C_0 - C_1}{2}\left(1 - \mathrm{erf}\left(\frac{x}{2\sqrt{Dt}}\right)\right)$, where $C(x,t)$ is the concentration in wt.% of the diffusing element C at distance x in m after time t in s and C_0 and C_1 are the initial concentrations of the diffusing element on either side of the couple. Fitting was performed by minimising the χ^2 misfit associated with the following function: $y_{est} = a\,\mathrm{erf}\big(b(x+c)\big) + d$, where y_{est} is the predicted concentration of a given oxide in wt.% and a, b, c and d are fitting parameters. The χ^2 misfit was defined as follows: $\chi^2 = \sum_{x=0}^{n}\left(\frac{(y_{obs} - y_{est})^2}{2\sigma}\right)$, where y_{obs} is the observed concentration of a given oxide in wt.% at a distance of x, y_{est} is the predicted concentration of a given oxide in wt.% at a distance of x and σ is the uncertainty associated with analyses of a given oxide in wt.%. Minimisations were performed with the fminsearch() function implemented in the pracma package of R[72]. Element diffusivities in m^2/s were then calculated using the following relationship[42]: $D = \frac{((1/b)^2)}{4t}$, where b is the fitting parameter described above.

Data availability

EMPA data and BSE maps are provided in the Supplementary Data.

References

1. Hofmann, A. W. & White, W. M. Mantle plumes from ancient oceanic crust. *Earth Planet. Sci. Lett.* **57**, 421–436 (1982).

2. Gast, P. W. Trace element fractionation and the origin of tholeiitic and alkaline magma types. *Geochim. Cosmochim. Acta* **32**, 1057–1086 (1968).

3. Hofmann, A. W. Mantle geochemistry: the message from oceanic volcanism. *Nature* **385**, 219–229 (1997).

4. Hirschmann, M. M. & Stolper, E. M. A possible role for garnet pyroxenite in the origin of the 'garnet signature' in MORB. *Contrib. to Mineral. Petrol.* **124**, 185–208 (1996).

5. Hauri, E. H. Major-element variability in the Hawaiian mantle plume. *Nature* **382**, 415–419 (1996).

6. Michael, P. J. & Chase, R. L. The influence of primary magma composition, H_2O and pressure on mid-ocean ridge basalt differentiation. *Contrib. to Mineral. Petrol.* **96**, 245–263 (1987).

7. Neave, D. A., Namur, O., Shorttle, O. & Holtz, F. Magmatic evolution biases basaltic records of mantle chemistry towards melts from recycled sources. *Earth Planet. Sci. Lett.* **520**, 199–211 (2019).

8. Maclennan, J. Concurrent mixing and cooling of melts under Iceland. *J. Petrol.* **49**, 1931–1953 (2008).

9. Shorttle, O. Geochemical variability in MORB controlled by concurrent mixing and crystallisation. *Earth Planet. Sci. Lett.* **424**, 1–14 (2015).

10. Rubin, K. H. & Sinton, J. M. Inferences on mid-ocean ridge thermal and magmatic structure from MORB compositions. *Earth Planet. Sci. Lett.* **260**, 257–276 (2007).

11. Saal, A. E., Hart, S. R., Shimizu, N., Hauri, E. H. & Layne, G. D. Pb isotopic variability in melt inclusions from oceanic island basalts, Polynesia. *Science (80-.).* **282**, 1481–1484 (1998).

12. Winpenny, B. & Maclennan, J. A partial record of mixing of mantle melts preserved in Icelandic phenocrysts. *J. Petrol.* **52**, 1791–1812 (2011).

13. Neave, D. A., Passmore, E., Maclennan, J., Fitton, J. G. & Thordarson, T. Crystal-melt relationships and the record of deep mixing and crystallization in the AD 1783 Laki eruption, Iceland. *J. Petrol.* **54**, 1661–1690 (2013).

14. Maclennan, J. Lead isotope variability in olivine-hosted melt inclusions from Iceland. *Geochim. Cosmochim. Acta* **72**, 4159–4176 (2008).

15. Kuo, L. C. & Kirkpatrick, R. J. Pre-eruption history of phyric basalts from DSDP legs 45 and 46: Evidence from morphology and zoning patterns in plagioclase. *Contrib. to Mineral. Petrol.* **79**, 13–27 (1982).

16. Dungan, M. A. & Rhodes, J. M. Residual Glasses and Melt Inclusions in Basalts from DSDP Legs 45 and 46: Evidence for Magma Mixing. *Contrib. to Mineral. Petrol.* **67**, 417–431 (1978).

17. Rhodes, J. M., Dungan, M. A., Blanchard, D. P. & Long, P. E. Magma mixing at mid-ocean ridges: evidence from basalts drilled near 22°N on the Mid-Atlantic Ridge. *Tectonophysics* **55**, 35–61 (1979).

18. Sobolev, A. V. & Shimizu, N. Ultra-depleted primary melt included in an olivine from the Mid-Atlantic Ridge. *Nature* **363**, 151–154 (1993).

19. Michael, P. J., McDonough, W. F., Nielsen, R. L. & Cornell, W. C. Depleted melt inclusions in MORB plagioclase: Messages from the mantle or mirages from the magma chamber? *Chem. Geol.* **183**, 43–61 (2002).

20. Neave, D. A., Hartley, M. E., Maclennan, J., Edmonds, M. & Thordarson, T. Volatile and light lithophile elements in high-anorthite plagioclase-hosted melt inclusions from Iceland. *Geochim. Cosmochim. Acta* **205**, 100–118 (2017).

21. van Gerve, T. D., Neave, D. A., Almeev, R. R., Holtz, F. & Namur, O. Zoned crystal records

of transcrustal magma transport, storage and differentiation: insights from the Shatsky Rise oceanic plateau. *J. Petrol.* **61**, egaa080 (2020).

22. Neave, D. A., Maclennan, J., Hartley, M. E., Edmonds, M. & Thordarson, T. Crystal storage and transfer in basaltic systems: the Skuggafjöll eruption, Iceland. *J. Petrol.* **55**, 2311–2346 (2014).

23. Bennett, E. N., Lissenberg, C. J. & Cashman, K. V. The significance of plagioclase textures in mid-ocean ridge basalt (Gakkel Ridge, Arctic Ocean). *Contrib. to Mineral. Petrol.* **174**, 49 (2019).

24. Kahl, M., Chakraborty, S., Costa, F. & Pompilio, M. Dynamic plumbing system beneath volcanoes revealed by kinetic modeling, and the connection to monitoring data: An example from Mt. Etna. *Earth Planet. Sci. Lett.* **308**, 11–22 (2011).

25. Mutch, E. J. F., Maclennan, J., Shorttle, O., Edmonds, M. & Rudge, J. F. Rapid transcrustal magma movement under Iceland. *Nat. Geosci.* **12**, 569–574 (2019).

26. Costa, F., Shea, T. & Ubide, T. Diffusion chronometry and the timescales of magmatic processes. *Nat. Rev. Earth Environ.* **1**, 201–214 (2020).

27. Ubide, T. & Kamber, B. S. Volcanic crystals as time capsules of eruption history. *Nat. Commun.* **9**, 326 (2018).

28. Kouchi, A. & Sunagawa, I. Mixing basaltic and dacitic magmas by forced convection. *Nature* **304**, 527–528 (1983).

29. De Campos, C. P., Dingwell, D. B. & Fehr, K. T. Decoupled convection cells from mixing experiments with alkaline melts from Phlegrean Fields. *Chem. Geol.* **213**, 227–251 (2004).

30. Kress, V. C. & Ghiorso, M. S. Multicomponent diffusion in MgO-Al_2O_3-SiO_2 and CaO-MgO-Al_2O_3-SiO_2 melts. *Geochim. Cosmochim. Acta* **57**, 4453–4466 (1993).

31. González-Garcia, D. *et al.* Diffusive exchange of trace elements between alkaline melts:

Implications for element fractionation and timescale estimations during magma mixing. *Geochim. Cosmochim. Acta* **233**, 95–114 (2018).

32. LaTourrette, T., Wasserburg, G. J. & Fahey, A. J. Self diffusion of Mg, Ca, Ba, Nd, Yb, Ti, Zr, and U in haplobasaltic melt. *Geochim. Cosmochim. Acta* **60**, 1329–1340 (1996).

33. Chen, Y. & Zhang, Y. Olivine dissolution in basaltic melt. *Geochim. Cosmochim. Acta* **72**, 4756–4777 (2008).

34. Chen, Y. & Zhang, Y. Clinopyroxene dissolution in basaltic melt. *Geochim. Cosmochim. Acta* **73**, 5730–5747 (2009).

35. Yu, Y., Zhang, Y., Chen, Y. & Xu, Z. Kinetics of anorthite dissolution in basaltic melt. *Geochim. Cosmochim. Acta* **179**, 257–274 (2016).

36. Shorttle, O. & Maclennan, J. Compositional trends of Icelandic basalts: Implications for short-length scale lithological heterogeneity in mantle plumes. *Geochemistry, Geophys. Geosystems* **12**, 1–32 (2011).

37. Neave, D. A. & Putirka, K. D. A new clinopyroxene-liquid barometer, and implications for magma storage pressures under Icelandic rift zones. *Am. Mineral.* **102**, 777–794 (2017).

38. Aranovich, L. Y. & Newton, R. C. Experimental determination of CO_2-H_2O activity-composition relations at 600-1000 °C and 6-14 kbar by reversed decarbonation and dehydration reactions. *Am. Mineral.* **84**, 1319–1332 (1999).

39. Botcharnikov, R. E., Koepke, J., Holtz, F., McCammon, C. & Wilke, M. The effect of water activity on the oxidation and structural state of Fe in a ferro-basaltic melt. *Geochim. Cosmochim. Acta* **69**, 5071–5085 (2005).

40. Zhang, Y., Walker, D. & Lesher, C. E. Diffusive crystal dissolution. *Contrib. to Mineral. Petrol.* **102**, 492–513 (1989).

41. Barr, J. A. & Grove, T. L. AuPdFe ternary solution model and applications to understanding

588 the fO_2 of hydrous, high-pressure experiments. *Contrib. to Mineral. Petrol.* **160**, 631–643
589 (2010).

590 42. Zhang, Y. Diffusion in minerals and melts: theoretical background. *Rev. Mineral.*
591 *Geochemistry* **72**, 5–59 (2010).

592 43. Lundstrom, C. C. An experimental investigation of the diffusive infiltration of alkalis into
593 partially molten peridotite: Implications for mantle melting processes. *Geochemistry, Geophys.*
594 *Geosystems* **4**, (2003).

595 44. Lowry, R. K., Henderson, P. & Nolan, J. Tracer diffusion of some alkali, alkaline-earth and
596 transition element ions in a basaltic and an andesitic melt, and the implications concerning
597 melt structure. *Contrib. to Mineral. Petrol.* **80**, 254–261 (1982).

598 45. Zhang, Y., Ni, H. & Chen, Y. Diffusion data in silicate melts. *Rev. Mineral. Geochemistry* **72**,
599 311–408 (2010).

600 46. Giordano, D., Russell, J. K. & Dingwell, D. B. Viscosity of magmatic liquids: A model. *Earth*
601 *Planet. Sci. Lett.* **271**, 123–134 (2008).

602 47. Glasstone, S., Laider, K. J. & Eyring, H. *The Theory of Rate Processes*. (McGraw-Hill, 1941).

603 48. Dingwell, D. B. Effects of structural relaxation on cationic tracer diffusion in silicate melts.
604 *Chem. Geol.* **82**, 209–216 (1990).

605 49. Mungall, J. E. Empirical models relating viscosity and tracer diffusion in magmatic silicate
606 melts. *Geochim. Cosmochim. Acta* **66**, 125–143 (2002).

607 50. Neave, D. A. *et al.* Clinopyroxene–liquid equilibria and geothermobarometry in natural and
608 experimental tholeiites: the 2014–2015 Holuhraun eruption, Iceland. *J. Petrol.* **60**, 1653–1680
609 (2019).

610 51. Cherniak, D. J. & Liang, Y. Ti diffusion in natural pyroxene. *Geochim. Cosmochim. Acta* **98**,
611 31–47 (2012).

612 52. Perugini, D., De Campos, C. P., Dingwell, D. B., Petrelli, M. & Poli, G. Trace element
613 mobility during magma mixing: Preliminary experimental results. *Chem. Geol.* **256**, 146–157
614 (2008).

615 53. Laeger, K. *et al.* High-resolution geochemistry of volcanic ash highlights complex magma
616 dynamics during the Eyjafjallajökull 2010 eruption. *Am. Mineral.* **102**, 1173–1186 (2017).

617 54. Kent, A. J. R. Melt inclusions in basaltic and related volcanic rocks. *Rev. Mineral.*
618 *Geochemistry* **69**, 273–331 (2008).

619 55. Dohmen, R. & Chakraborty, S. Fe-Mg diffusion in olivine II: Point defect chemistry, change
620 of diffusion mechanisms and a model for calculation of diffusion coefficients in natural
621 olivine. *Phys. Chem. Miner.* **34**, 409–430 (2007).

622 56. Caricchi, L. *et al.* A Data Driven Approach to Investigate the Chemical Variability of
623 Clinopyroxenes From the 2014–2015 Holuhraun–Bárdarbunga Eruption (Iceland). *Front.*
624 *Earth Sci.* **8**, 1–15 (2020).

625 57. Lange, A. E., Nielsen, R. L., Tepley, F. J. & Kent, A. J. R. The petrogenesis of plagioclase-
626 phyric basalts at mid-ocean ridges. *Geochemistry, Geophys. Geosystems* **14**, 3282–3296
627 (2013).

628 58. Holness, M. B. *et al.* Textures in partially solidified crystalline nodules: A window into the
629 pore structure of slowly cooled mafic intrusions. *J. Petrol.* **48**, 1243–1264 (2007).

630 59. Bergantz, G. W., Schleicher, J. M. & Burgisser, A. Open-system dynamics and mixing in
631 magma mushes. *Nat. Geosci.* **8**, 793–796 (2015).

632 60. Halldórsson, S. A. *et al.* Isotopic-heterogeneity of the Thjorsa lava-Implications for mantle
633 sources and crustal processes within the Eastern Rift Zone, Iceland. *Chem. Geol.* **255**, 305–316
634 (2008).

635 61. Lange, A. E., Nielsen, R. L., Tepley, F. J. & Kent, A. J. R. Diverse Sr isotope signatures
636 preserved in mid-oceanic-ridge basalt plagioclase. *Geology* **41**, 279–282 (2013).

637 62. Grove, T. L., Kinzler, R. J. & Bryan, W. B. Fractionation of Mid-Ocean Ridge Basalt
638 (MORB). in *Mantle Flow and Melt Generation at Mid-Ocean Ridges, Geophysical*
639 *Monograph 71* 281–310 (American Geophysical Union, 1992).

640 63. O'Neill, H. S. C. & Jenner, F. E. The global pattern of trace-element distributions in ocean
641 floor basalts. *Nature* **491**, 698–704 (2012).

642 64. Costa, F., Coogan, L. A. & Chakraborty, S. The time scales of magma mixing and mingling
643 involving primitive melts and melt-mush interaction at mid-ocean ridges. *Contrib. to Mineral.*
644 *Petrol.* **159**, 371–387 (2010).

645 65. Ridley, I. W., Perfit, M. R., Smith, M. C. & Fornari, D. J. Magmatic processes in developing
646 oceanic crust revealed in a cumulate xenolith collected at the East Pacific Rise, 9°50'N.
647 *Geochemistry, Geophys. Geosystems* **7**, Q12O04 (2006).

648 66. Sisson, T. W. & Grove, T. L. Experimental investigations of the role of H_2O in calc-alkaline
649 differentiation and subduction zone magmatism. *Contrib. to Mineral. Petrol.* **113**, 143–166
650 (1993).

651 67. Gaetani, G. A. & Grove, T. L. The influence of water on melting of mantle peridotite. *Contrib.*
652 *to Mineral. Petrol.* **131**, 323–346 (1998).

653 68. Husen, A., Almeev, R. R. & Holtz, F. The Effect of H_2O and Pressure on Multiple Saturation
654 and Liquid Lines of Descent in Basalt from the Shatsky Rise. *J. Petrol.* **57**, 309–344 (2016).

655 69. Berndt, J. *et al.* A combined rapid-quench and H_2-membrane setup for internally heated
656 pressure vessels: Description and application for water solubility in basaltic melts. *Am.*
657 *Mineral.* **87**, 1717–1726 (2002).

658 70. Erdmann, M. & Koepke, J. Experimental temperature cycling as a powerful tool to enlarge
659 melt pools and crystals at magma storage conditions. *Am. Mineral.* **101**, 960–969 (2016).

660 71. Jarosewich, E., Nelen, J. A. & Norberg, J. A. Reference samples for electron microprobe
661 analysis. *Geostand. Newsl.* **4**, 43–47 (1980).

662 72. R Development Core Team. R: A Language and Environment for Statistical Computing. *R*
663 *Found. Stat. Comput.* (2016).

664 **Acknowledgements**

665 We thank Ulrich Kroll and Stefan Linsler for their help with maintaining IHPV equipment, and Renat
666 Almeev and Chao Zhang for their help with EPMA. This work and DAN were supported by the
667 German Research Foundation (DFG; NE2097/1-1). DAN was also supported Presidential Fellowship
668 from the University of Manchester and a NERC Independent Research Fellowship (NE/T011106/1).

669 **Author contributions**

670 DAN designed the project. PB performed the experiments and EPMA analyses under the supervision
671 of DAN and FH. HB performed the FTIR analyses. All authors contributed to data interpretation.
672 DAN wrote the manuscript with contributions from PB, HB and FH.

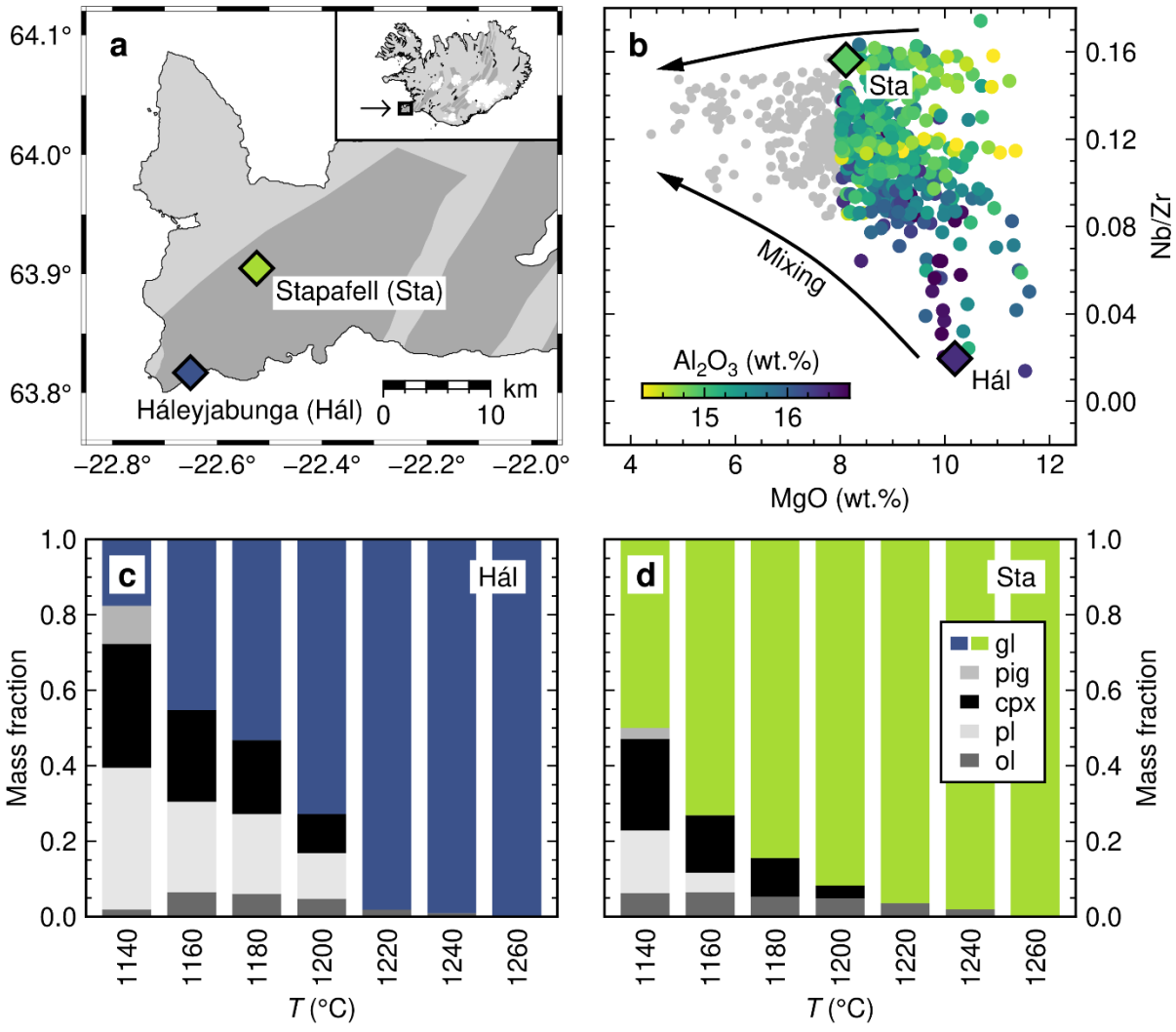

673

674 **Fig. 1 Mantle-derived chemical variability in Icelandic basalts and its effects on the phase**
675 **equilibria relations of primitive magmas. a** Locations of the incompatible element-depleted
676 Háleyjabunga (Hál) and incompatible element-enriched Stapafell (Sta) lavas on the Reykjanes
677 Peninsula of southwest Iceland. **b** Summary of major and trace element variability in lavas from
678 southwest Iceland[36]. MgO reflects the degree of magmatic evolution and Nb/Zr the degree of mantle-
679 derived incompatible element enrichment. At any given MgO content, incompatible element-enriched
680 lavas like those from Stapafell have lower Al_2O_3 contents than incompatible-element depleted lavas
681 like those from Háleyjabunga. Arrows illustrate the reduction in chemical variability that results from
682 concurrent mixing and crystallisation during magmatic evolution[8,9]. **c, d** Phase equilibria relations of
683 Háleyjabunga (**c**) and Stapafell (**d**) lava analogues derived from crystallisation experiments at
684 300 MPa[7]. Equilibrium phase assemblages and proportions are related to the degree of incompatible

element enrichment: plagioclase crystallises at higher temperatures and in greater amounts from incompatible element-depleted magmas that are correspondingly enriched in refractory elements like CaO and Al_2O_3. Phases are labelled as follows: gl, glass; pig, pigeonite; cpx, clinopyroxene; pl, plagioclase; and ol, olivine.

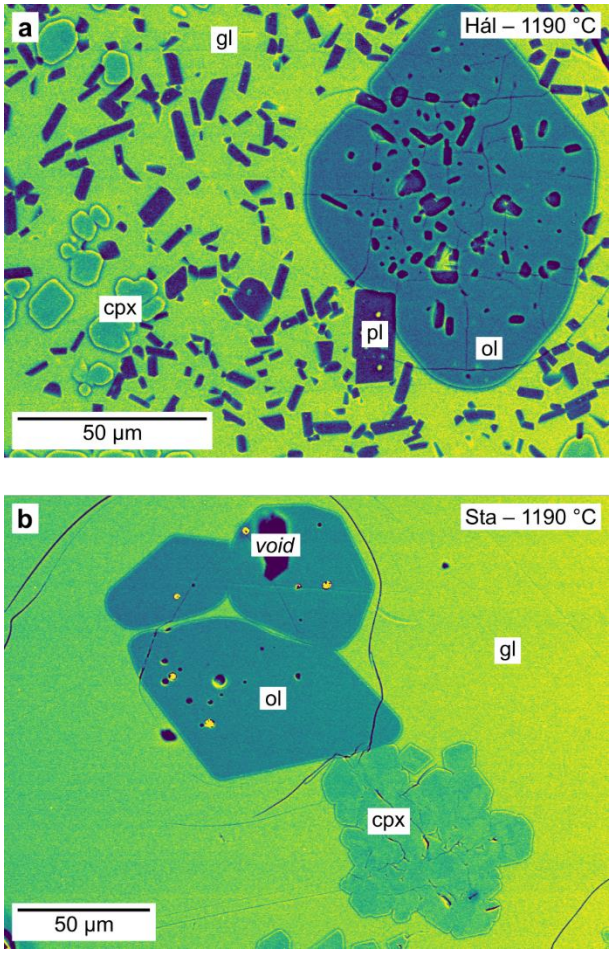

Fig. 2 Backscattered electron (BSE) images of the products of synthesis experiments. Synthesis experiments were performed on Háleyjabunga and Stapafell lava analogues at 300 MPa and 1190 °C. These conditions were chosen to maximise differences in equilibrium phase assemblages and proportions[7]. **a** Products of the synthesis experiment on the incompatible element-depleted Háleyjabunga (Hál) lava analogue contain crystals of olivine (ol), clinopyroxene (cpx) and plagioclase (pl) in relatively modest amounts of glass [gl; melt mass fraction (F) ~ 0.72]. **b** Products of the synthesis experiment on the incompatible element-enriched Stapafell (Sta) lava analogue contain crystals olivine (ol), clinopyroxene (cpx) in relatively large amounts of glass (gl; F ~ 0.90).

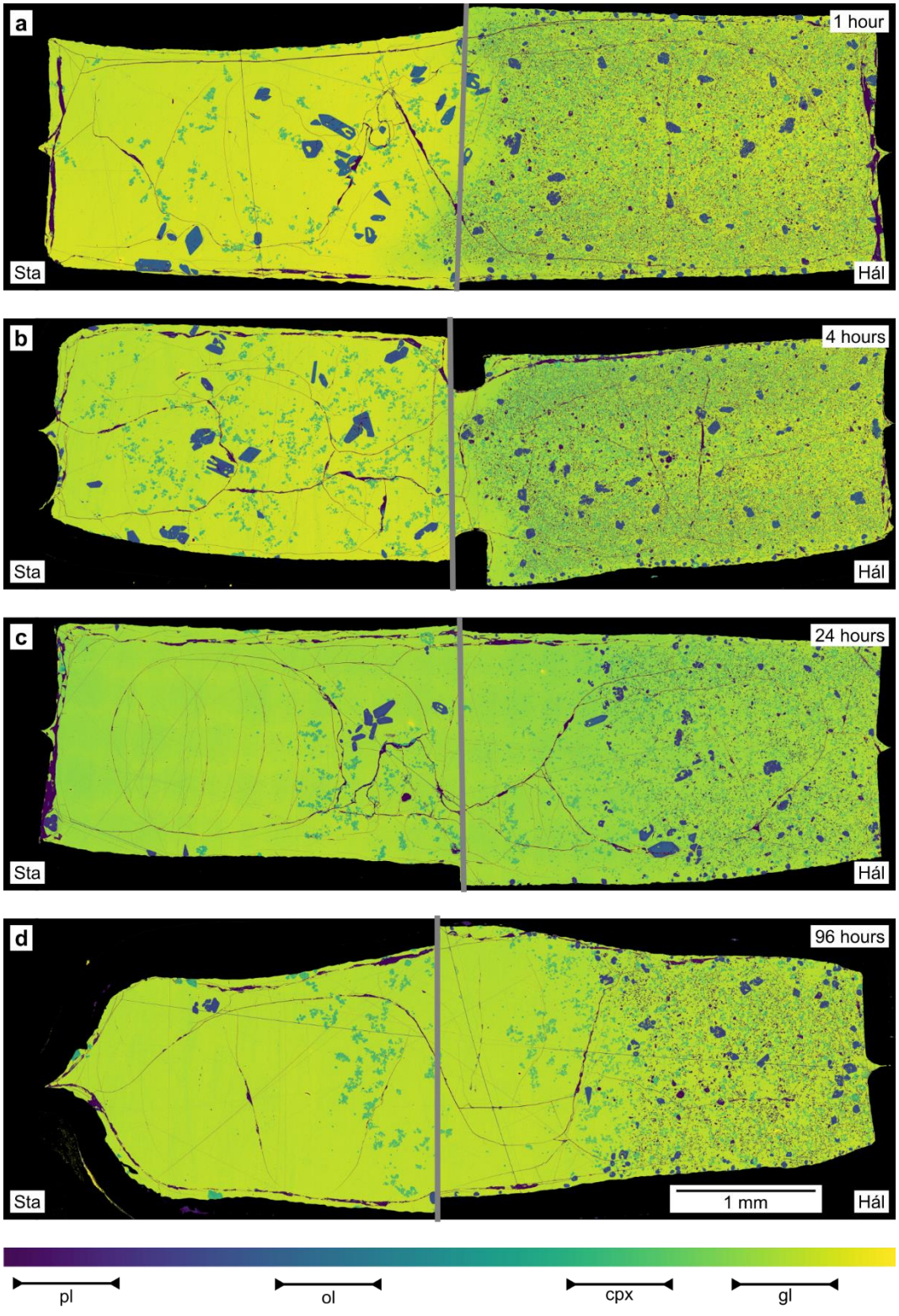

Fig. 3 Backscattered electron (BSE) maps of the products of magma-magma reaction experiments. Magma-magma reaction experiments were performed by juxtaposing quenched magma cylinders from synthesis experiments on both Háleyjabunga (Hál) and Stapafell (Sta) lava analogues within new capsules. These new capsules were then subjected to exactly the same conditions used

during synthesis experiments (300 MPa and 1190 °C). **a-d** BSE maps show the products of experiments run for 1 hour (**a**), 4 hours (**b**), 24 hours (**c**) and 96 hours (**d**). Magma cylinders synthesised from the incompatible element-depleted Háleyjabunga lava analogue are on the right, and magma cylinders synthesised from the incompatible element-enriched Stapafell lava analogue are on the left. Grey lines show the positions of original interfaces between juxtaposed magma cylinders. Plagioclase (pl) is the lowest BSE intensity phase (purple, only towards the right), followed, in order of increasing intensity, by olivine (ol, blue), clinopyroxene (cpx, blue-green) and glass (gl, green to yellow).

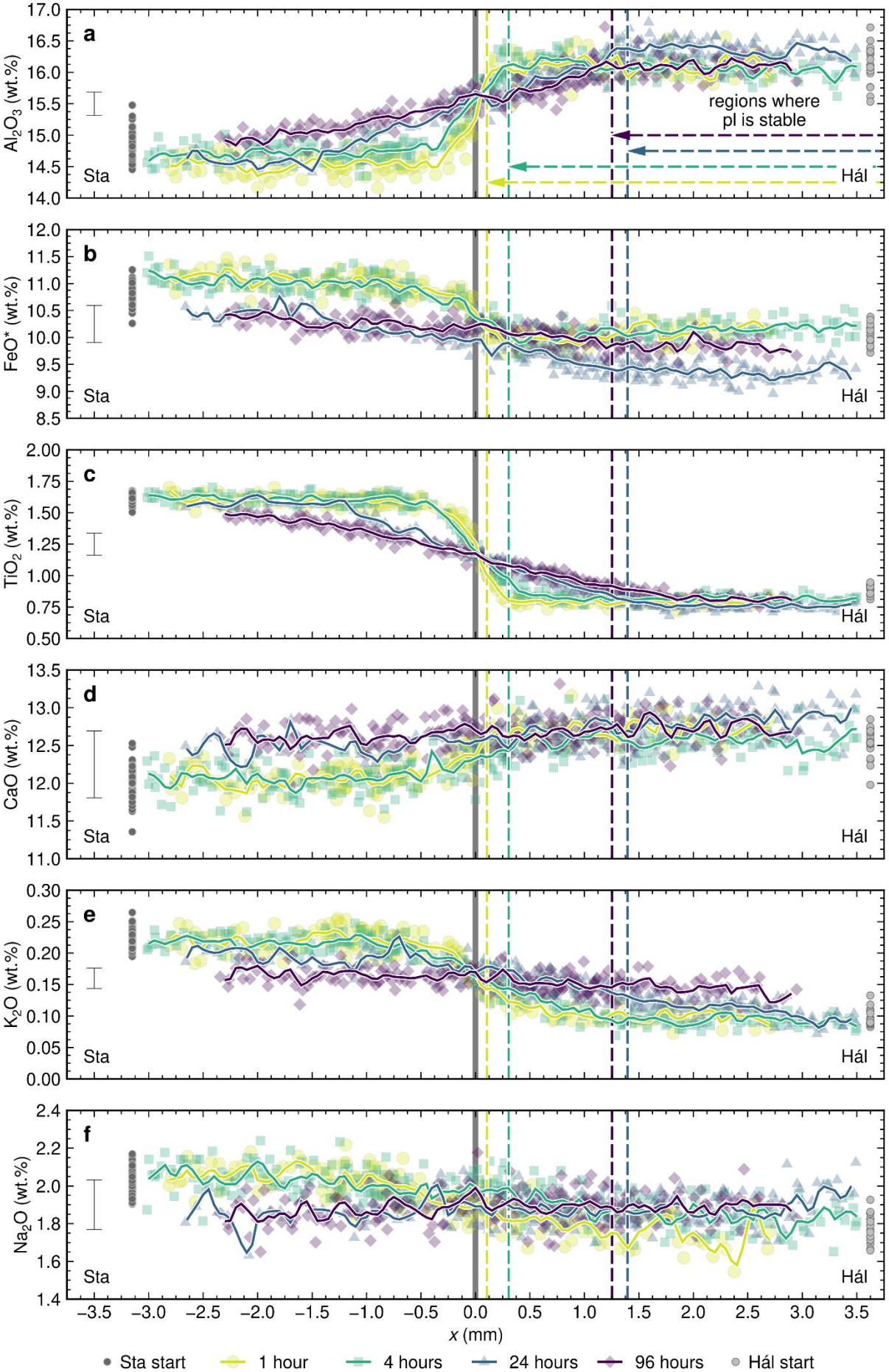
a
b
c
d
e
f
Al2O3 (wt.%)
FeO* (wt.%)
TiO2 (wt.%)
CaO (wt.%)
K2O (wt.%)
Na2O (wt.%)
Sta
Hál
regions where
pl is stable
x (mm)
Sta start
1 hour
4 hours
24 hours
96 hours
Hál start

Fig. 4 Glass composition profiles through the products of magma-magma reaction experiments. Glass composition profiles are centred on the interfaces between juxtaposed magma cylinders, which are indicated by vertical grey lines. Analyses from the products of experiments with different durations are shown with different colours and symbols. Solid lines show moving averages calculated by applying a Gaussian filter with a 0.25 mm bandwidth to the raw analyses. Regions of the experimental products where plagioclase (pl) is stable are shown with dashed vertical lines and horizontal arrows. Compositions of glasses in the products of synthesis experiments are shown with grey symbols. Characteristic 2σ analytical uncertainties are shown. **a-f** Glass composition profiles are shown in order of increasing element diffusivity[45]: Al_2O_3 (**a**), FeO* (**b**), TiO_2 (**c**), CaO (**d**), K_2O (**e**) and Na_2O (**f**). No analyses are shown for SiO_2 or MgO because along-profile compositional variability does not exceed analytical uncertainty for these elements (Supplementary Data). **a-c** Relatively slow-diffusing elements typically show composition profiles with sigmoidal shapes for all experimental durations. Sigmoidal profiles are especially clear in the cases of Al_2O_3 (**a**) and TiO_2 (**c**) but obfuscated by Fe-loss for experimental durations ≥24 hours in the case of FeO* (**b**). **d-f** Relatively fast-diffusing elements only show composition profiles with sigmoidal shapes for short experimental durations. This is emphasised most by Na_2O (**f**) for which all initial variability is erased within 24 hours.

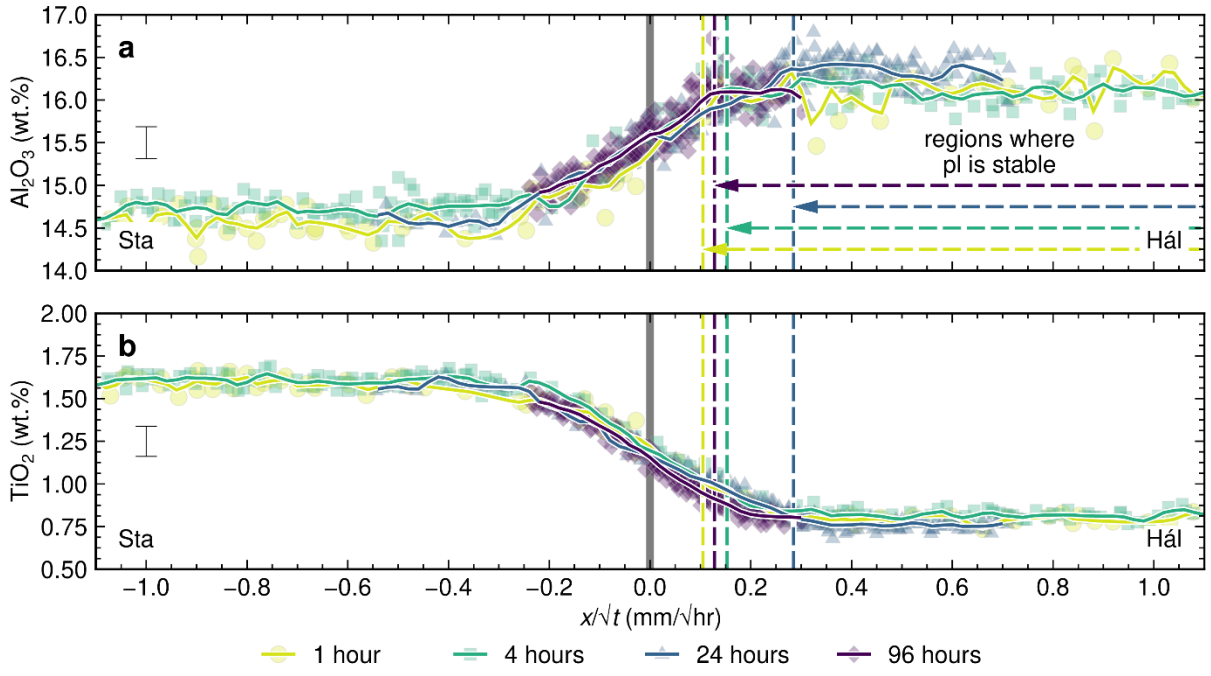

728

729 **Fig. 5 Time-normalised glass composition profiles through the products of magma-magma**
730 **reaction experiments.** Normalising glass composition profiles by the square roots of experimental
731 durations eliminates the effects of time on the evolution of diffusively controlled composition
732 profiles, which thus collapse onto single curves for each element[31,45]. Symbols are the same as in Fig.
733 4. **a, b** Closely overlapping time-normalised glass compositions profiles for Al_2O_3 (**a**) and TiO_2 (**b**)
734 confirm that diffusion in experimental melts was the dominant process controlling chemical
735 variability in the products of our magma-magma reaction experiments.

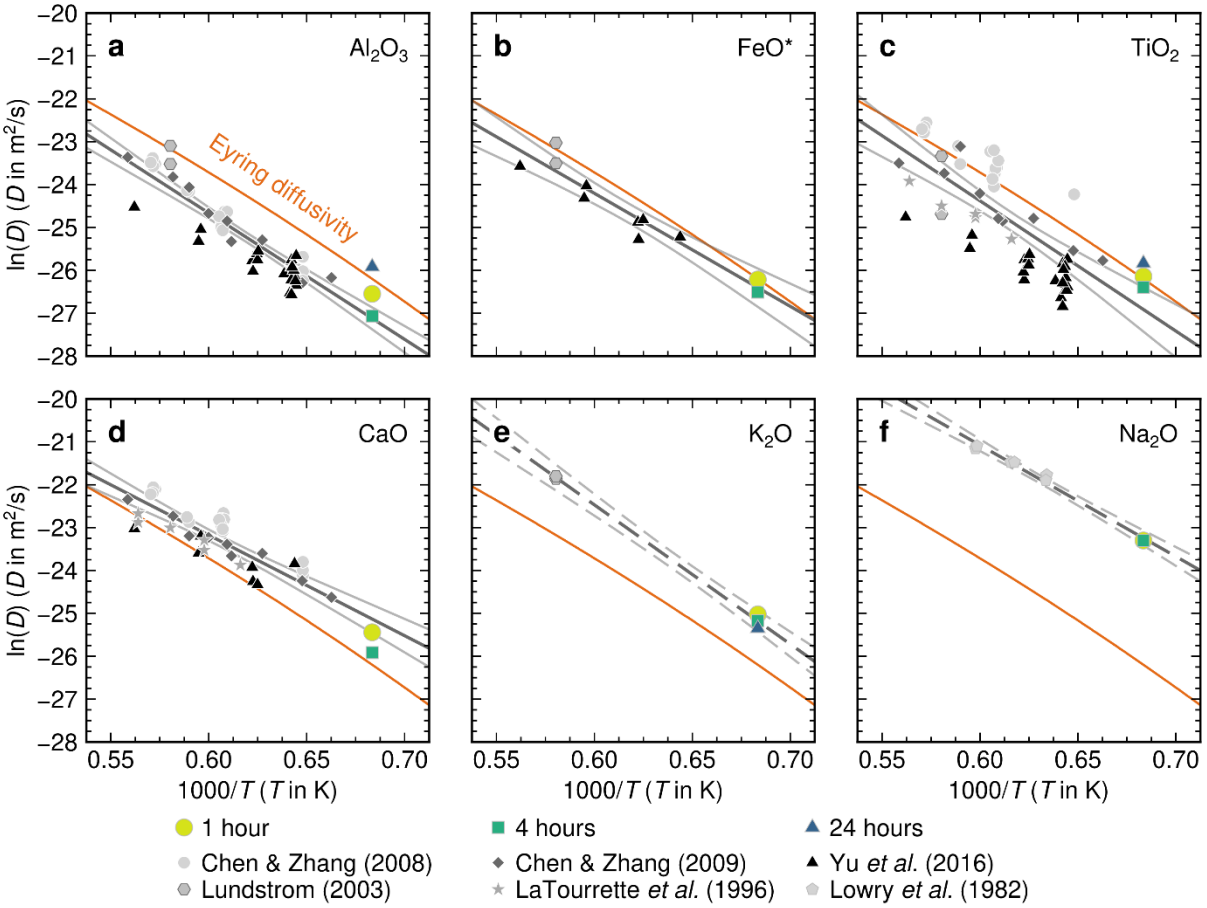

Fig. 6 Element diffusivities in basaltic melts. Effective binary diffusion coefficients (*D*) were estimated by fitting error functions to glass composition profiles to solve Fick's 2nd Law, and are summarised in 1000/*T* versus ln(*D*) space alongside published diffusivities from experiments on basaltic systems[32–35,43,44]. Diffusion coefficients estimated from our experiments are only presented for element-duration combinations for which composition profiles have clearly sigmoidal forms. Temperature- and viscosity-dependent Eyring diffusivities calculated with a characteristic diffusive jump length of 0.4 nm are shown as orange lines[31,47]. Grey lines show regressions with 95% confidence intervals through global datasets. Dashed lines show tentative regressions for elements with sparse diffusion data. **a** Estimated Al_2O_3 diffusivities are broadly consistent with Eyring diffusivities and slightly faster than predicted from published diffusivities[33–35,43]. **b** Estimated FeO* diffusivities are similar to Eyring diffusivities and consistent with published diffusivities[35,43] **c** Estimated TiO_2 diffusivities are similar to Eyring diffusivities and consistent with many published diffusivities, though published values span up to three ln units at any given temeprature[32–35,43]. **d**

Estimated CaO diffusivities are slightly faster than Eyring diffusivities but appear slightly slower than published diffusivities[32–35]. **e** Estimated K_2O diffusivities are a ln unit faster than Eyring diffusivities but define a plausible array in $1000/T$ versus $\ln(D)$ space with the limited number of published diffusivities available[43]. **f** Estimated Na_2O diffusivities are three ln units faster than Eyring diffusivities. They are also coherent with some published diffusivities[44], but not others[34].

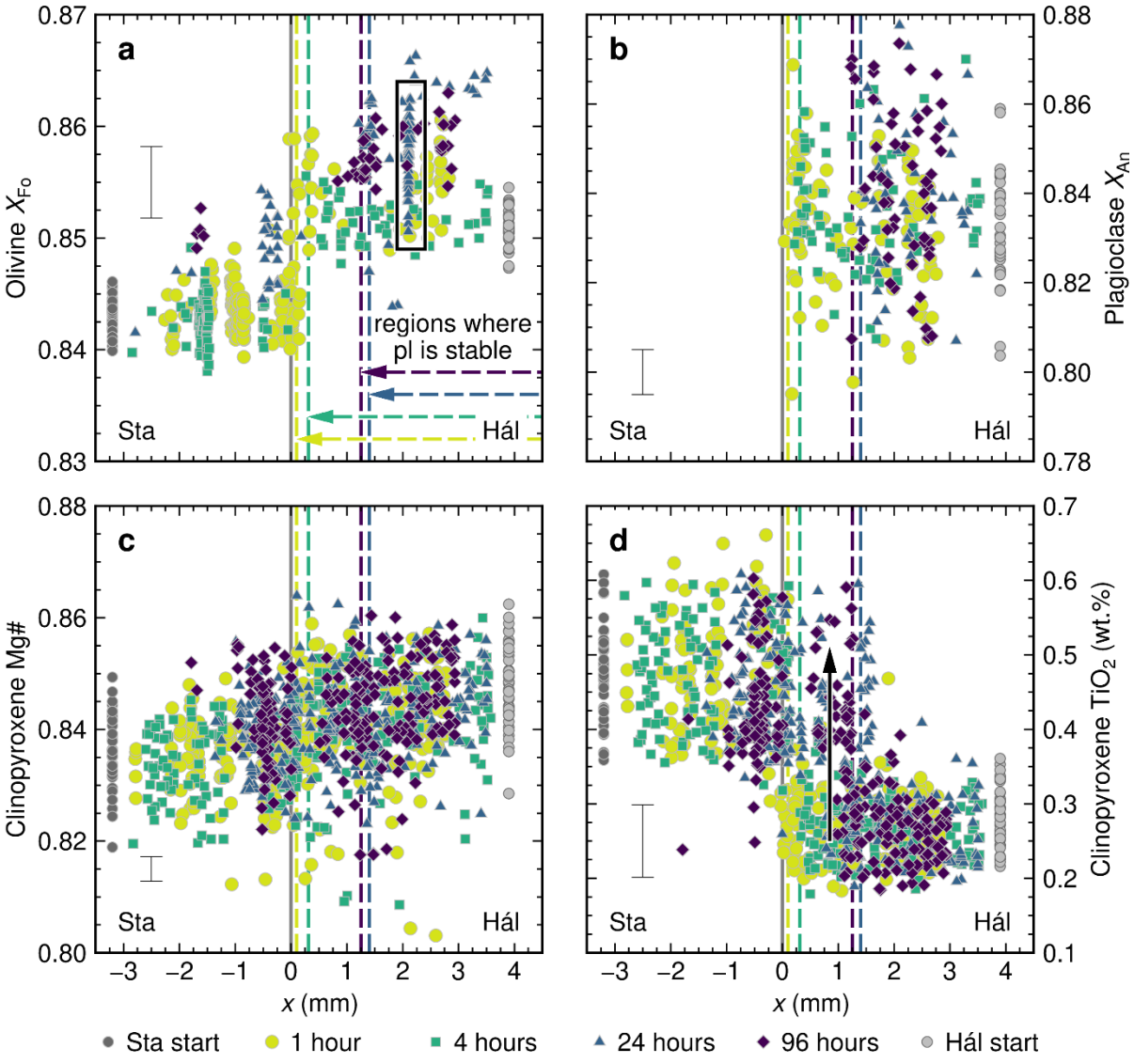

Fig. 7 Distribution of crystal compositions in the products of magma-magma reaction experiments. The positions of interfaces between juxtaposed magma cylinders are shown as vertical grey lines. Regions of the experimental products within which plagioclase (pl) is stable are shown with dashed vertical lines and horizontal arrows. Compositions of minerals in the products of synthesis experiments are shown with grey symbols. Characteristic 2σ analytical uncertainties are shown. **a** Distribution of olivine compositions across the products of magma-magma reaction experiments summarised in terms of olivine forsterite content [X_{Fo}, where X_{Fo} = Mg/(Mg+Fe) on molar a basis]. Steps in X_{Fo} across interfaces between magma analogues reflect the higher FeO* content of the incompatible element-enriched Stapafell lava analogue with respect to the incompatible element-depleted Háleyjabunga analogue. Iron loss and diffusive re-equilibration of melt FeO*

766 contents triggered the diffusive re-equilibration of X_{Fo} in some crystals (one example is outlined in
767 black box). **b** Distribution of plagioclase compositions across the products of magma-magma reaction
768 experiments summarised in terms of plagioclase anorthite content [X_{An}, where X_{An} = Ca/(Ca+Na) on a
769 molar basis]. The region where plagioclase is stabile contracts significantly as a function of increasing
770 experimental duration as a result of plagioclase resorption in response to diffusively driven changes in
771 melt compositions. Although X_{An} is somewhat variable, potentially as a consequence of
772 disequilibrium crystallisation during the initial phases of synthesis experiments, it does not vary
773 systematically with position or experimental duration. **c** Distribution of clinopyroxene compositions
774 across the products of magma-magma reaction experiments summarised in terms of clinopyroxene
775 Mg-number [$Mg\#_{cpx}$, where $Mg\#_{cpx}$ = Mg/(Mg+Fe) on a molar basis]. While much of variability in
776 $Mg\#_{cpx}$ reflects the development of clinopyroxene sector zoning[50], mean $Mg\#_{cpx}$ contents are slightly
777 higher in the FeO*-poor Háleyjabunga analogue than the FeO*-rich Stapafell analogue. **d** Distribution
778 of clinopyroxene compositions across the products of magma-magma reaction experiments
779 summarised in terms of clinopyroxene TiO_2 contents. Clinopyroxene crystals from the incompatible
780 element-enriched Stapafell analogue are richer in TiO_2 than those from the incompatible element-
781 depleted Háleyjabunga analogue. Moreover, clinopyroxene crystals within regions of plagioclase
782 resorption have high TiO_2 contents, suggesting that plagioclase resorption is spatially correlated with
783 the resorption and re-crystallisation of clinopyroxene, as indicated by the black arrow.

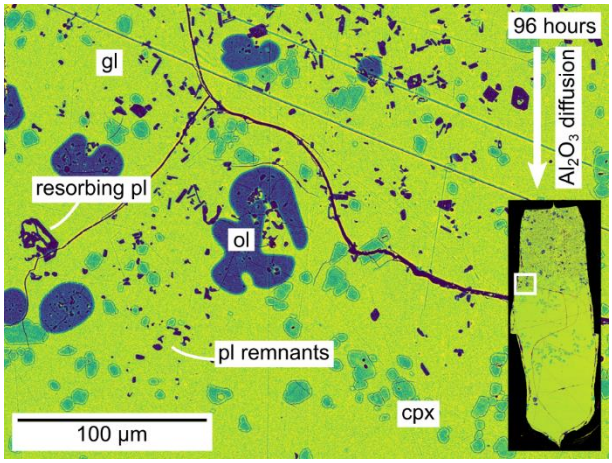

Fig. 8 Backscattered electron (BSE) image showing plagioclase resorption in the products of the 96-hours magma-magma reaction experiment. Many plagioclase (pl) crystals close to plagioclase resorption fronts show resorbed, and the last remnants of resorbing plagioclase crystals are especially irregular. Some olivine (ol) crystals close to plagioclase resorption fronts are anhedral and embayed, whereas clinopyroxene (cpx) crystals retain euhedral to subhedral textures.

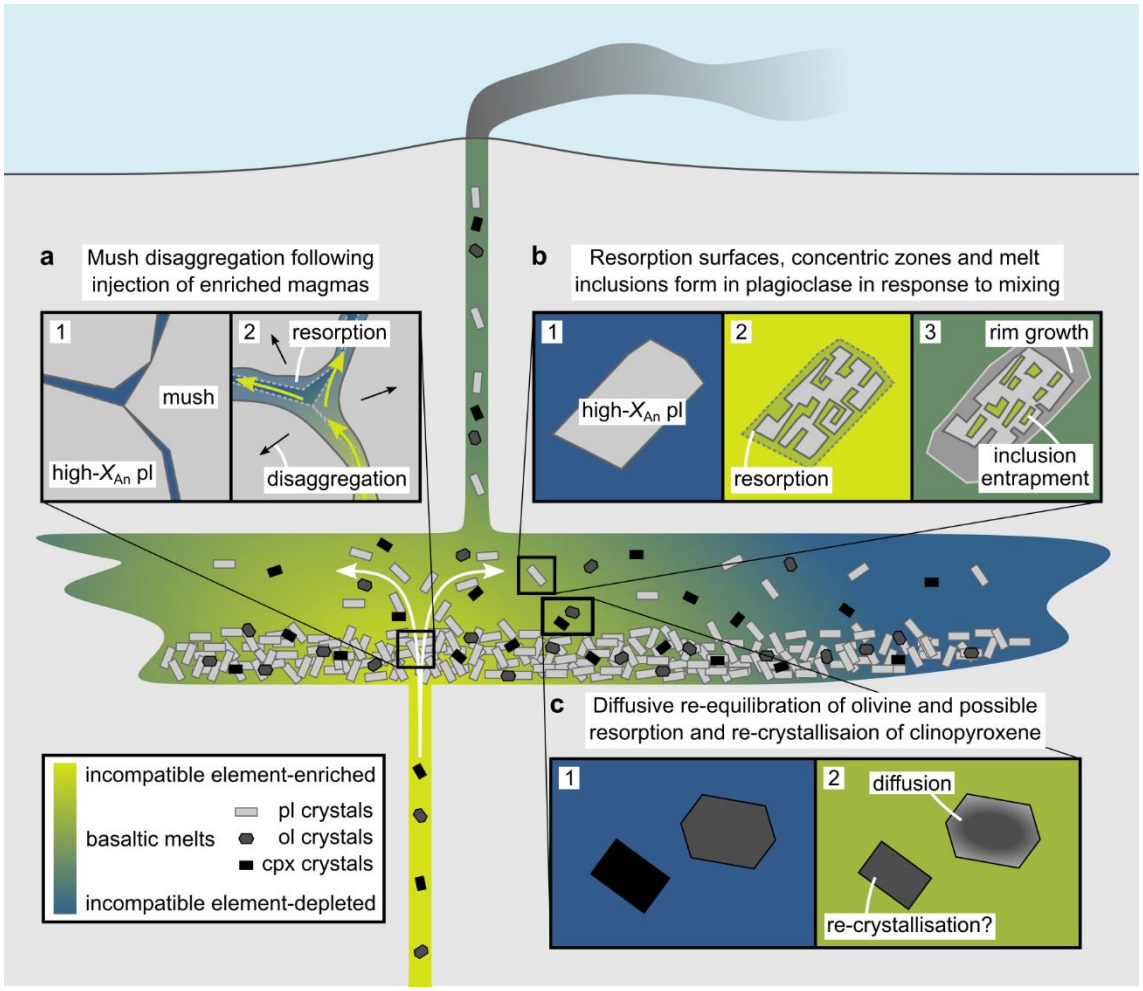

Fig. 9 Cartoon summarising how mixing-induced chemical disequilibrium creates and modifies basaltic crystal cargoes. Primitive and incompatible element-depleted magmas crystallise high-anorthite [high-X_{An}, where X_{An} = Ca/(Ca+Na) on a molar basis] plagioclase (pl) alongside olivine (ol) and clinopyroxene (cpx) during storage in the crust[7,62]. Even under isothermal conditions, recharge by incompatible element-enriched and plagioclase-undersaturated primitive magmas can trigger changes in the crystalline portions of incompatible element-depleted and plagioclase-saturated magma reservoirs. **a** The infiltration of plagioclase-dominated mushes by plagioclase-undersaturated magmas may trigger mush disaggregation by resorbing grain boundaries, as indicated by chemical and isotopic disequilibria between some basaltic melts and their cargoes of high-X_{An} plagioclase crystals[22,60]. **b** The transfer of high- X_{An} plagioclase crystals between variably incompatible element-enriched magmas that are also variably saturated in plagioclase produces resorption surfaces, concentric zoning, overgrowth rims and melt inclusions[19,20,23]. **c** Olivine and clinopyroxene crystals may re-equilibrate,

803 and resorb and re-crystallise, respectively, in response to isothermal mixing of variably incompatible
804 element-enriched magmas with different major element compositions.